Journal of Catalysis 263 (2009) 292–305

Contents lists available at ScienceDirect

Journal of Catalysis

www.elsevier.com/locate/jcat

Nanofibrous γ-Al_2O_3 as support for Co-based Fischer–Tropsch catalysts: Pondering the relevance of diffusional and dispersion effects on catalytic performance

Agustín Martínez *, Gonzalo Prieto, Joan Rollán

Instituto de Tecnología Química, UPV-CSIC, Avda. de los Naranjos s/n, 46022 Valencia, Spain

ARTICLE INFO

Article history:
Received 29 August 2008
Revised 16 January 2009
Accepted 20 February 2009

Keywords:
Fischer–Tropsch
RuCo/alumina catalysts
Hierarchical macro-mesoporous
Nanofibrous alumina
Cobalt dispersion and diffusional effects

ABSTRACT

Hierarchical macro-mesoporous nanofibrous γ-alumina (Al_2O_3_nf) synthesized by a surfactant-templated route has been applied for the first time as support for preparing RuCo catalysts at two different loading levels (20 wt% Co–0.5 wt% Ru and 30 wt% Co–1.0 wt% Ru). Equivalent catalysts involving four commercial aluminas (Sasol, mean pore size ranging from 6.0 to 32.4 nm) have also been prepared for comparison purposes. The materials have been exhaustively characterized (XRD, elemental analysis, ICP-OES, N_2 physisorption, Hg intrusion porosimetry, TEM-HRTEM, FE-SEM, H_2 chemisorption, and H_2-TPR) and evaluated for Fischer–Tropsch synthesis (FTS) in a fixed-bed reactor under realistic conditions. Nanofibrous alumina displayed simultaneously the highest specific surface area (321 m^2/g) and the largest macroporosity. The introduction of the original nanofibrous morphology allowed us to conclude that Co dispersion is mainly driven by support surface area rather than by pore size. By taking advantage of these properties, RuCo/Al_2O_3_nf catalysts bearing both the highest metal dispersion and macroporosity have been used in this work to ponder the relevance of dispersion and intrapellet diffusion on FTS catalyst performance, which is of paramount importance for designing improved Co-based FTS catalysts. While initial (TOS $\rightarrow$ 0) FTS rates were related to cobalt dispersion through the recently reported particle size–TOF dependence, *pseudo*-steady-state FTS activity and selectivity were dictated by both dispersion and support porosity, evidencing the kinetic relevance of CO and α-olefin intrapellet diffusion through the liquid phase filling the catalyst pores under working conditions. At high metal loadings, where the relative population of intrinsically less active and C_{5+} selective Co^0 nanoparticles is decreased, RuCo/Al_2O_3_nf catalyst displayed the highest cobalt-time-yield and diesel productivity.

1. Introduction

The Fischer–Tropsch synthesis (FTS) is a well-established technology permitting the upgrading of abundant natural gas and coal as well as renewable biomass resources into liquid fuels and valuable chemicals through conversion of syngas (CO + H_2) [1–3]. In particular, ultra-high quality diesel can be obtained through the selective hydrocracking of waxes produced in low-temperature FTS preferably using a Co-based catalyst [4,5]. In these catalysts, a high density of active Co^0 sites is ensured by spreading a suitable cobalt precursor onto a porous inorganic carrier, among which SiO_2, Al_2O_3, and TiO_2 (to a lesser extent) are the most widely applied in commercial catalyst formulations [6]. The final density of Co^0 sites is determined by the cobalt loading, metal dispersion, and the extent of cobalt reduction attained upon catalyst activation treatments. Cobalt dispersion and reducibility depends on the metal–support interaction strength [7] which, for the three most commonly used supports, decreases in the following order: TiO_2 > Al_2O_3 > SiO_2. Addition of small amounts (<1.5 wt%) of easily reducible noble or semi-noble metals, such as Ru, Re, and Pt, is of common practice in commercial catalyst formulations in order to enhance cobalt reducibility through H_2 spillover effects [8]. Alumina, particularly when used in its γ-Al_2O_3 crystalline phase, displays an intermediate Co–support interaction strength thus combining a relatively high capacity for dispersing the cobalt phases as compared to SiO_2 with a moderate formation of barely reducible species in comparison to the more interacting TiO_2 support [7]. In addition, alumina based FTS catalysts display good mechanical properties and thus a high resistance to attrition [9], a property that is of particular concern in slurry bubble column reactors (SBCR) whose optimization in the last decades has significantly contributed to the development of more efficient FTS technologies [10].

In the steady state, a catalyst working under realistic FTS conditions (high CO conversion and high selectivity to waxes) has its pores filled with liquid hydrocarbons and this certainly introduces constraints to the diffusion of reactants (CO) and products

* Corresponding author. Fax: +34 963877808.
E-mail address: amart@itq.upv.es (A. Martínez).

0021-9517/$ – see front matter
doi:10.1016/j.jcat.2009.02.021

(α-olefins) through the dense liquid phase which might have an impact on catalyst performance [11–13]. Under conditions of CO-limited diffusion, a CO concentration profile is established between the gas phase and the Co^0 particle inside the pore increasing the actual H_2/CO ratio at the surrounding of the active site. A positive dependence of the chain-insertion elementary kinetic step on CO partial pressure and a faster hydrogenation of the adsorbed intermediates at higher H_2/CO ratios determine an enhanced selectivity to lighter hydrocarbons under CO-limited diffusion conditions. On the other hand, increasing the restrictions for the diffusion of α-olefins through the dense liquid phase filling the pores increases the probability for their re-adsorption on Co^0 sites and insertion into the growing chains, enhancing the formation of long-chain hydrocarbons [13]. Diffusional issues in FTS have been nicely gathered by Iglesia and co-workers [13,14] who, by using adimensional analysis, arrived to a structural parameter (χ) which mainly depends on the volumetric density of active sites (and thus indirectly on the support porosity, surface area, and metal loading), the average pore size, and the size of the catalyst pellets. Since the size of the catalyst pellets is often determined by the reactor hydrodynamics, only the catalyst pore size and surface area are left as degrees of freedom in the design of improved FTS catalysts, for instance, by taking advantage of recent developments in the synthesis of advanced porous materials. For inorganic solids with conventional morphologies (as those typically used as supports for cobalt) of nearly round particles having intraparticle porosity consisting of a network of cylindrical pores, surface area and pore size are not independent parameters and thus any improvement in surface area is necessarily accompanied by a decrease in the mean pore size. In this case, the expected advantages of using high surface area supports (i.e. increased metal dispersion) could be partially lost owing to a large proportion of small size pores through which a restricted CO diffusion may decrease the steady-state activity and shift the product distribution toward less desired lighter hydrocarbons.

It clearly follows from the above considerations that an interesting approach for the development of improved Co-based FTS catalysts could be the use of advanced inorganic porous supports with particular morphology that may avoid the surface area–pore size interdependence typical of conventional morphologies. If this can be achieved, the use of catalysts based on such novel support morphologies is also expected to shed light on the relative impact of metal particle size and diffusion-related processes on catalyst performance under real FTS conditions. Cobalt particle size effects have been, indeed, a matter of intense study in the literature [15–18], though in supported cobalt catalysts with conventional morphology those effects may be obscured by diffusion-related effects as the mean cobalt particle size is always influenced by the size of the support pores confining the metal particles [19]. Pondering the relevance of these two important parameters, i.e. particle size and pore size, on catalyst performance is of paramount importance for designing improved Co-based FTS catalysts in terms of optimized metal dispersion and texture. In this respect, the usually called one-dimensional (1D) morphologies have recently become attainable at the nanoscale level (nanowires, nanorods, nanofibers or nanotubes) for a wide variety of inorganic oxides using hard [20,21] and soft [22–24] templating approaches. Though most of these oxides displayed valuable features as catalysts and catalytic supports already in the form of nanosized powders, the novel 1D morphology has shown to deeply modify their characteristics leading, in some cases, to materials with enhanced catalytic properties [25–27]. The templated-1D morphology at a nanoscale level might bring about new materials combining high surface areas along with a large (macro)porosity [28], in opposition to conventional morphologies with exclusively intraparticle porosity. Due to its wide range of applications as absorbent, binder and catalytic carrier, the templated synthesis of γ-Al_2O_3 has been extensively studied in the more recent years [22–24,29,30]. Different approaches have been used to synthesize γ-Al_2O_3 with nanofibrous morphology. Commonly, long-chain surfactants are used to force sol–gel synthesis to occur in the confinement of longitudinal micelles in the presence [23] or in the absence [22] of organic solvents. Other methodologies are based on hydrothermal treatments on pre-synthesized nanosized $Al(OH)_x$ solids in the presence of surfactants through the so called "surfactant-induced fiber formation" [24,31]. The later approach avoids the use of organic solvents and allows the synthesis of boehmite precursors of Al_2O_3 at much softer temperatures than those involving a sol–gel process in the presence of surfactants.

The present study addresses the implications of using a macro-mesoporous nanofibrous γ-Al_2O_3 material as support on the physicochemical and catalytic properties of Co-based catalysts for FTS. Several commercial γ-Al_2O_3 (Sasol) covering a wide range of pore sizes from 6 up to 32 nm have been used as reference supports in order to put the nanofibrous catalysts in proper perspective. The advantages introduced by the original macro-mesoporosity and 1D primary particle morphology for the supporting γ-Al_2O_3 phase in terms of pondering the relevance of cobalt particle size and porosity-related diffusion phenomena on the FTS catalytic performance are discussed. The implications of the acquired knowledge on the design of improved FTS catalysts are also examined.

2. Experimental

2.1. Preparation of catalysts

2.1.1. Nanofibrous and commercial aluminas

Nanofibrous γ-Al_2O_3 was prepared according to a procedure previously reported [24] with slight modifications. Specifically, a 0.2 M solution of $Al(NO_3)_3$ (Aldrich) in deionized water was dropwise added (1 mL/min) to a NH_4Cl (2 M)/NH_4OH (2 M) buffer solution (pH = 10.5) in order to precipitate $Al(OH)_x$. Aluminum nitrate was used here as precursor instead of $NaAlO_2$ as reported in the original work by Zhu et al. [24] in order to avoid the presence of Na in the final catalysts that, even at the ppm level, might have a deleterious affect on the FTS performance [32]. The white precipitate was filtered and thoroughly washed with deionized water until no chloride was detected in the outgoing waters. Then, the wet cake was mixed with the non-ionic surfactant $C_{11-15}H_{23-31}O(CH_2CCH_2O)H$ commercially known as Tergitol 15-TS-7 (Aldrich) in a molar ratio $Al(OH)_3$:surfactant:H_2O of 1:0.4:160. The mixture (pH = 7–7.3) was loaded in Teflon-lined autoclaves and hydrothermally treated at 373 K in static for 48 hours. The product (pH = 3.5–4) was diluted in deionized water, alkalinized with a NH_3 (25 wt%) aqueous solution (Acros) until pH = 9 and the solid recovered by centrifugation, dried at 333 K overnight, and finally calcined in a muffle oven at 773 K for 20 h (heating rate 2 K/min) to remove the remaining surfactant and to crystallize the boehmite nanofibers into the γ-Al_2O_3 phase.

Four high-purity commercial aluminas were kindly supplied by Sasol in the form of powders and used in this work for comparison purposes. Two of the samples (Catapal-B and Pural-SB) are commercialized in the form of boehmite and pseudo-boehmite and thus were submitted to a calcination step at 773 K for 10 hours in a muffle oven in order to obtain the corresponding γ-Al_2O_3 forms. The remaining samples (Puralox TH100/150 and Catalox HTa101) were already received as γ-Al_2O_3 and used without any further treatment.

The following nomenclature has been applied for the commercial and nanofibrous γ-Al_2O_3 solids: Al_2O_3_1 (derived from

Catapal-B), Al_2O_3_2 (derived from Pural-SB), Al_2O_3_3 (Puralox TH100-150), Al_2O_3_4 (Catalox HTa101), and Al_2O_3_nf (nanofibrous).

2.1.2. RuCo/γ-Al_2O_3 catalysts

RuCo/γ-Al_2O_3 catalysts were obtained by impregnation of the alumina supports (45–65 μm particle size), previously dried at 423 K for 12 h, with an excess (10 mL/g) of aqueous solution of $Co(NO_3)_2{\cdot}6H_2O$ (Aldrich) and ruthenium (III) nitrosyl nitrate solution (1.5 wt% Ru, Aldrich). The dried solids were suspended in the solution containing the Co and Ru precursors and the mixture stirred at room temperature for 1 h. Then, the water solvent was removed in a rotary evaporator at 323 K and the solids dried at 343 K under vacuum for an additional hour. The samples were further dried in an oven at 373 K overnight and finally calcined at 573 K for 3 h in flowing air by increasing the temperature at a heating rate of 1 K/min in order to promote the slow decomposition of the metal precursors. By adjusting the amount of precursors in the mixed solution, two series of catalysts with different nominal Co and Ru loadings were prepared: (a) series 20% Co/Al_2O_3_x containing 0.5 wt% Ru and 20 wt% Co, and (b) series 30% Co/Al_2O_3_x loaded with 1 wt% Ru and 30 wt% Co, where $x = 1$–4 or nf according to the nomenclature applied for the different aluminas.

2.2. Characterization techniques

2.2.1. ICP-OE spectrometry and elemental analysis

The amount of Co and Ru in the calcined catalysts, as well as in selected samples before calcination (dried) and after catalysis (spent), was determined by ICP-OES in a Varian 715-ES spectrometer after complete dissolution of the solids (ca. 20 mg) in a HNO_3/HF/HCl solution (1/1/3 volume ratio).

Elemental analysis was also performed on selected dried and calcined samples in order to determine the nitrogen content. The analyses were performed in a Fisons EA1108 instrument using sulfanilamide as standard.

2.2.2. N_2 physisorption

The N_2 adsorption–desorption isotherms for the γ-Al_2O_3 supports and the corresponding RuCo/γ-Al_2O_3 catalysts were measured in a Micromeritics ASAP 2000 equipment. The samples (ca. 200 mg) were degassed at 673 K for 24 h prior to analysis. Specific surface areas were estimated by using the B.E.T. approach. Average pore sizes and pore size distributions were obtained by applying the B.J.H. formalism to the adsorption branch of the isotherms, according to the IUPAC recommendations for solids with an hysteresis loop deviating from type H1, as it is the case here for some of the wide pore alumina supports, and for solids with certain pore blockage as it occurs for the metal-loaded CoRu/alumina catalysts [33].

2.2.3. Hg intrusion porosimetry

The macroporosity (pores larger than 50 nm) of selected samples was assessed by mercury intrusion porosimetry in a Fisons Pascal 240 porosimeter. A contact angle of 141° and a cylindrical pore model were considered for the calculations. The samples (ca. 100 mg, 45–65 μm particle size) were dried at 353 K overnight and then degassed *in situ* at room temperature and 0.2 mbar before measurement.

2.2.4. X-ray diffraction

X-ray diffraction patterns were acquired at room temperature in a Phillips X'pert diffractometer using monochromatized CuK_α radiation. The average crystal size of the supports was determined by applying the Scherrer's equation to the (4 0 0) diffraction of γ-Al_2O_3. The average particle size of Co_3O_4 in calcined catalysts was estimated from the Scherrer's equation applied to the most intense (3 1 1) diffraction ($2\theta = 36.9°$) using a shape factor $K = 0.9$. The mean Co^0 particle size in reduced catalysts was then obtained from the corresponding Co_3O_4 particle size by applying the molar volume correction [34]:

$$d(Co^0) = (3/4)d(Co_3O_4).$$

2.2.5. Temperature-programmed reduction

The reduction behavior of the supported metal oxide phases was studied by hydrogen temperature-programmed reduction (H_2-TPR) in a Micromeritics Autochem 2910 apparatus. About 30 mg of sample were initially flushed with an Ar flow at room temperature (RT) for 30 min, then the gas was switched to 10 vol% H_2 in Ar and the temperature increased up to 1173 K at a heating rate of 10 K/min. The H_2 consumption rate was monitored in a thermal conductivity detector (TCD) previously calibrated using the reduction of CuO as reference.

The extent of cobalt reduction was determined using the equipment described above as follows: about 100 mg of sample were reduced in the U-shaped cell at 673 K (heating rate 1 K/min) for 10 h in flowing pure H_2 (50 cm^3/min), that is, the same reduction conditions applied prior to catalysis. Then, the H_2 gas was switched to Ar and the sample was flushed at 673 K for 30 min. Afterward, the flowing gas was changed to 10 vol% H_2 in Ar and the temperature linearly increased from 673 K up to 1173 K at a heating rate of 10 K/min while monitoring the H_2 consumption in a TCD. It is assumed that the reduction of RuO_x to Ru^0 and Co_3O_4 to CoO proceeded quantitatively during the 10 h treatment and, thus, that the H_2 consumed in the H_2-TPR of the pre-reduced sample (673–1173 K) is exclusively due to the further reduction of CoO to Co^0. This assumption is supported by the H_2-TPR profiles of the calcined catalysts, as will be shown later. For estimating the degree of reduction, it was also assumed that complete reduction of Co_3O_4 to Co^0 took place during the H_2-TPR of calcined samples (RT–1173 K), as confirmed from the total amount of H_2 consumed and the Co content determined by ICP-OES. The degree of reduction (DG, in %) is then estimated as:

$$\text{DG } (\%) = (1 - F/T) \cdot 100,$$

where F is the amount of Co that has been reduced during the TPR of the pre-reduced (673 K for 10 h) sample and T is the total amount of cobalt. The degrees of reduction determined by the above procedure are subjected to an experimental error (2σ) of ±2.8%, as calculated from three independent measurements on the 20% Co/Al_2O_3_nf sample.

2.2.6. Hydrogen chemisorption

Cobalt dispersions were determined for the 20% Co/Al_2O_3_x series by H_2 chemisorption at 423 K in an ASAP 2010C Micromeritics equipment by extrapolating the total gas uptakes in the H_2 adsorption isotherms at zero pressure, following in detail the procedure reported by Bartholomew et al. [35]. Prior to adsorption, the samples (ca. 0.5 g) were pre-treated in flowing He at 393 K for 1 h. Afterward, the samples were reduced *in situ* by flowing pure H_2 and raising the temperature from 393 K to 673 K at a heating rate of 1 K/min and maintaining this temperature for 10 h. After reduction, the samples were degassed at 1.3 Pa and the temperature lowered to 423 K. Co^0 particle sizes were estimated from the total (reversible + irreversible) amount of chemisorbed H_2, Co content (from ICP-OES), and extent of cobalt reduction (at 673 K/10 h) by assuming a H/Co = 1 atomic ratio stoichiometry and a hemispherical particle geometry with a surface atomic density of 14.6 atoms/nm^2.

2.2.7. Electron microscopy

Transmission electron microscopy (TEM and HRTEM) characterization of selected samples was performed in a *Tecnai G² field emission gun* (200 kV) device equipped with EDAX microanalysis. Before TEM observation, the samples were prepared by suspending the solid in ethanol and submitting the suspension to ultrasonication for one minute. Afterward, the suspension was let to slowly decant for two minutes and a drop was extracted from the top side and placed on a holly carbon-coated copper grid. RuCo/alumina catalysts were previously reduced in flowing pure H_2 for 10 h at 673 K and stored under a $<1\%$ O_2/N_2 passivating atmosphere until sample preparation for microscopy.

Scanning electron micrographs (SEM) have been recorded in a Hitachi S-4100 field-emission (FE) gun microscope equipped with a BSE-AUTRATA detector using gold-coated powder specimens.

2.3. Fischer–Tropsch synthesis

The Fischer–Tropsch synthesis (FTS) was carried out in a downflow fixed-bed stainless steel reactor, as detailed elsewhere [36,37]. In a typical experiment, the reactor was loaded with 1.0–1.5 g of catalyst in the calcined form (0.25–0.42 mm pellet size) previously diluted with the required amount of silicon carbide (0.6–0.8 mm) to attain a constant bed volume of 6.4 cm^3. Then, the catalyst was reduced *in situ* at atmospheric pressure in flowing pure H_2 (200 $cm^3/(min\, g_{cat})$) at 673 K for 10 h (1 K/min heating rate). After reduction the temperature was lowered down to 373 K under the flow of H_2, and subsequently a flow of a mixture of CO, H_2, and Ar (CO:H_2:Ar volume ratio of 3:6:1, Ar used as internal standard) was established through the reactor, the reaction pressure slowly increased up to 2.0 MPa, and the temperature raised up to 493 K at a rate of 4 K/min. Under these conditions a *pseudo*-steady catalytic behavior was usually attained at time-on-stream (TOS) above 7–8 h. A constant gas hourly space velocity (GHSV) of 7.2 $L_{syngas}/(g_{cat}\, h)$ was applied for all catalysts during the first 7–8 h on stream (transient period) and then the space velocity was adjusted in each case to attain a *pseudo*-steady CO conversion of 40%. The temperature in the catalyst bed was controlled to 493 ± 1 K by means of two independent electric heating zones, with the corresponding temperature controllers connected to thermocouples located in different positions inside the catalytic bed. An additional movable thermocouple was used to verify the absence of longitudinal temperature gradients and hot spots along the catalyst bed. During the reaction, heavy hydrocarbons (C_{15+}) were condensed in two consecutive traps located at the reactor outlet and kept at 423 and 373 K, respectively, both at the reaction pressure of 2.0 MPa. The product stream leaving the second trap was depressurized and analyzed on line at periodic intervals in a GC (Varian 3800) equipped with three columns and two detectors [37]. The heavier products accumulated in the two traps were removed after the transient (TOS $\sim$ 7 h) and *pseudo*-steady (TOS $\sim$ 15 h) periods, weighted, diluted with CS_2, and analyzed in the same GC. Carbon mass balances obtained independently for the two periods were quite satisfactory ($100 \pm 2\%$). Product yields and selectivities are given on a carbon basis.

3. Results and discussion

3.1. Properties of the catalytic alumina supports

3.1.1. Nitrogen physisorption

As seen in Fig. 1, all the alumina supports display non-reversible adsorption–desorption isotherms with an hysteresis loop characteristic of capillary condensation in mesopores (2–50 nm). The isotherms of samples Al_2O_3_1, Al_2O_3_2, and Al_2O_3_3 tend to reach a plateau above a certain relative pressure, indicating that most of the pores in these solids fall within the mesopore range. The relative pressure at which the plateau is attained increases from $P/P_0 = 0.87$ for Al_2O_3_1 to 0.97 for Al_2O_3_3 reflecting the increase in the mean size of the mesopores. A distinct behavior can be perceived at high relative pressures ($P/P_0 > 0.9$) in the N_2 isotherms of Al_2O_3_4 and Al_2O_3_nf aluminas. For these two solids, a plateau above a certain relative pressure is not longer observed and, instead, both the adsorption and desorption branches continuously increase until saturation ($P/P_0 = 1$).

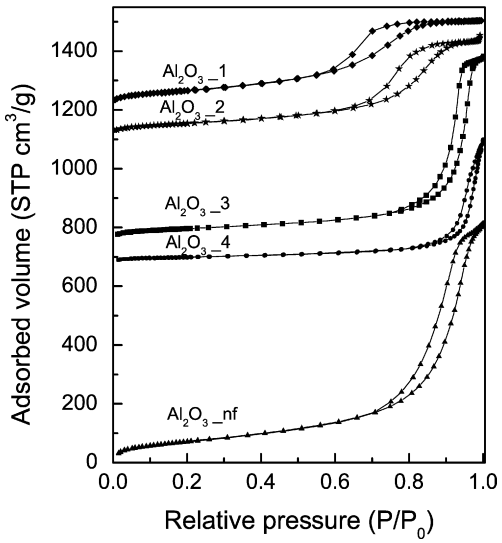

Fig. 1. N_2 physisorption isotherms for commercial (Al_2O_3_1–Al_2O_3_4) and nanofibrous (Al_2O_3_nf) aluminas. Isotherms for Al_2O_3_(1–4) have been offset vertically by 1200, 1100, 750 and 650 cm^3/g, respectively.

The hysteresis loops in Al_2O_3_1, Al_2O_3_2, and Al_2O_3_3 can be classified as type *H2* according to the IUPAC recommendations for gas physisorption data analysis [33] and suggest the presence of nearly tubular mesopores with a relatively narrow pore size distribution. Conversely, the shape of the hysteresis loops in Al_2O_3_4 and Al_2O_3_nf falls within *H3* and *H4* categories [33], which are typical of slit-type pores associated to the interparticle porosity generated in solids having plate or fiber-like morphology. This suggests that the latter two solids might contain larger pores with diameters beyond those measurable by N_2 physisorption, as will be discussed later on the basis of Hg porosimetry data.

Fig. 2 depicts the pore size distributions in the 2–200 nm range obtained from the absorption branch of the N_2 isotherms by applying the B.J.H. formalism. According to N_2 physisorption all alumina supports display an unimodal pore size distribution with mean pore sizes ranging from 6.0 nm (Al_2O_3_1) to 32.4 nm (Al_2O_3_4). The nanofibrous Al_2O_3_nf material presents an intermediate mean pore diameter of 16.1 nm. Table 1 summarizes the textural properties of the alumina supports. As seen there, the B.E.T. surface area of the commercial aluminas shows a descending trend from 254 to 70 m^2/g with increasing the mean pore diameter from 6.0 to 32.4 nm, evidencing the inverse relationship between pore size and surface area typical of inorganic porous oxides with conventional morphologies (i.e. intraparticle porosity). This trend does not apply at all for the nanofibrous alumina which displays the highest specific surface area (321 m^2/g) and total pore volume (1.29 cm^3/g) and an intermediate pore size of 16.1 nm according to N_2 physisorption.

3.1.2. Mercury intrusion porosimetry

The presence of macropores in the nanofibrous sample and in selected commercial aluminas was assessed by means of mercury intrusion porosimetry. As seen in Table 1, the volume of macropores (>50 nm in diameter) in Al_2O_3_2 and Al_2O_3_3 (0.04 and

Table 1
Origin and textural properties of the γ-alumina supports.

Support	Origin	N_2 physisorption			Hg intrusion PV[c] (cm^3/g)	Crystal size (nm)
		B.E.T. (m^2/g)	PD[a] (nm)	PV[b] (cm^3/g)		
Al_2O_3_1	Catapal-B (Sasol)	254	6.0	0.48	–	3.9
Al_2O_3_2	Pural-SB (Sasol)	192	9.1	0.55	0.04	4.2
Al_2O_3_3	Puralox TH100/150 (Sasol)	157	21.8	0.98	0.09	7.0
Al_2O_3_4	Catalox HTa101 (Sasol)	70	32.4	0.65	0.11	8.5
Al_2O_3_nf	Nanofibrous γ-Al_2O_3	321	16.1	1.29	0.26	3.5

[a] Mean pore diameter estimated from the absorption branch of the isotherm by applying the B.J.H. formalism.
[b] Total pore volume.
[c] Total pore volume for pores in the range of 50–10^3 nm diameter as determined by Hg intrusion porosimetry.

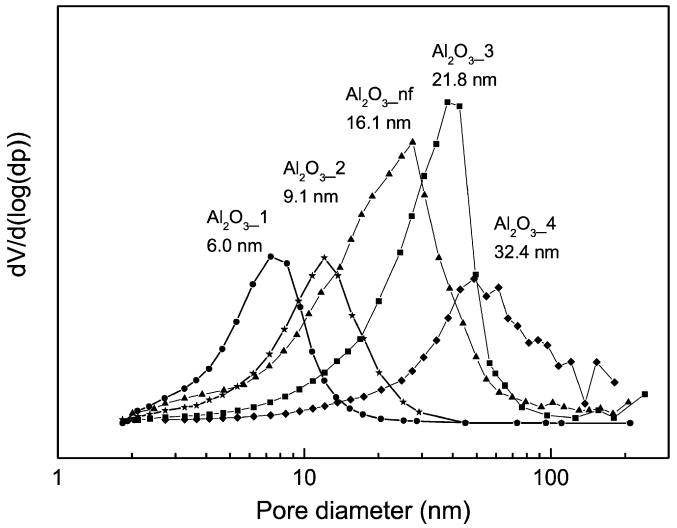

Fig. 2. Pore size distributions for the commercial (Al_2O_3_1–Al_2O_3_4) and nanofibrous (Al_2O_3_nf) aluminas obtained by applying the B.J.H. formalism to the adsorption branch of the N_2 isotherms.

0.09 cm^3/g, respectively) is less than 10% the total pore volume determined by N_2 physisorption, indicating a negligible contribution of macropores to the total porosity in these solids, as it was predicted from the shape of their respective N_2 hysteresis loops (Fig. 1). The relative contribution of macropores is expected to be even lower for Al_2O_3_1 with the smallest average pore size. This result concurs with that published by others on similar commercial aluminas obtained from the same supplier (Sasol) [32]. On the other hand, the macropore volume of Al_2O_3_4 determined by Hg intrusion amounts to 0.11 cm^3/g, although it has to be kept in mind that, as it is evidenced in Fig. 2, part of the macropores (those in the 50–200 nm range) in this sample are already accounted for in the total pore volume determined by N_2 physisorption. It is worth to mention here that the volume corresponding to mesopores measured by Hg intrusion fits reasonably well with that obtained by N_2 physisorption. According to Hg intrusion measurements, the nanofibrous Al_2O_3_nf sample bears the largest macropore volume (0.26 cm^3/g) and thus the highest relative contribution of macropores to the total porosity taking into account that this sample contains almost no macropores in the range covered by N_2 physisorption (Fig. 2). Therefore, the nanofibrous alumina should be described by a bimodal pore size distribution with mesopores and macropores averaging 16.1 nm and 240 nm in size, respectively. Due to its bimodal porosity, we believe that using only the mean mesopore size determined by N_2 adsorption may not be appropriate for describing the porosity of Al_2O_3_nf because the detected macropores could dramatically influence the intrapellet transport rates during FTS, as will be seen later when discussing the catalytic results. Moreover, a single mean pore size value (obtained for instance by combining the N_2 physisorption and Hg intrusion results) will not be assumed for Al_2O_3_nf as it may not be rigorous for describing the mentioned bimodal porosity. Therefore, the macro-mesoporous nanofibrous alumina will be hereafter considered as the widest pore alumina support without assigning it a definite mean pore size ($d_p \gg 40$ nm) just to account for the significant contribution of macropores and to avoid misleading conclusions when the physicochemical and catalytic properties of the corresponding CoRu catalysts are put in perspective with those based on the commercial aluminas. For the latter materials, however, the average pore size given by N_2 physisorption will be used for describing their porosity for sake of clarity, even if Hg porosimetry revealed a certain contribution of macropores to the total porosity of Al_2O_3_4.

3.1.3. X-ray diffraction

The only crystalline phase detected by X-ray diffraction in all the alumina supports after the calcination treatment at 773 K, when required (see Section 2.1.1), was γ-Al_2O_3. The corresponding crystallite sizes estimated from the (4 0 0) reflection of γ-Al_2O_3 are included in Table 1. As observed, the crystallite size of the γ-Al_2O_3 phase in the commercial aluminas decreases from 8.5 to 3.9 nm when decreasing the mean pore size, which is in accord with the increase in surface area. On the other hand, the Al_2O_3_nf sample displays the smallest crystallite size (3.5 nm) thus stressing the nanocrystalline nature of this material synthesized in the confinement of nanosized domains delimited by the surfactant molecules.

3.1.4. Electron microscopy (TEM and SEM)

The texture of the pristine γ-Al_2O_3 supports has been studied by TEM. Representative TEM images of the four commercial aluminas are shown in Fig. S1 of the supporting information. The narrow pore Al_2O_3_1 and Al_2O_3_2 samples consist in worm-like nanocrystallites assembled in a porous network (Figs. S1a and S1b, respectively). The size of the individual particles increments from 2–3 × 7–15 nm in Al_2O_3_1 (pore size of 6.0 nm) to 3–5 × 10–25 nm in Al_2O_3_2 (pore size of 9.1 nm). The size is further increased to 7–12 × 25–40 nm in the rod-like primary particles found in Al_2O_3_3 (Fig. S1c) having an average pore size of 21.8 nm. On the other hand, the widest pore Al_2O_3_4 commercial alumina consists of larger parallelepiped particles, showing also intraparticle voids (Fig. S1d), which assemble in an open network, consistent with the existence of macropores as found by Hg porosimetry. Finally, a representative bright-field TEM image at medium magnification of the nanofibrous alumina is shown in Fig. 3. As seen there, Al_2O_3_nf consists of very long nanofibers (2–3 × 20–50 nm) displaying by far the highest aspect ratio within all the aluminas studied. The nanofibers are randomly packed with low density allowing for the existence of large interparticle voids consistent with the presence

Table 2
Chemical composition and textural properties of RuCo/alumina catalysts.

Catalyst	Co content (wt%)	Ru content (wt%)			Nitrogen content (wt%)		B.E.T. (m^2/g)	PV (cm^3/g)	PD (nm)
		Dried	Calcined	Spent	Dried	Calcined			
20% Co/Al_2O_3_1	20.7	0.58	0.28	0.24	5.1	0.3	196	0.35	5.9
20% Co/Al_2O_3_2	22.1	0.52	0.27	0.25	5.3	0.4	181	0.36	7.1
20% Co/Al_2O_3_3	22.3	0.50	0.28	0.27			127	0.58	15.1
20% Co/Al_2O_3_4	21.7		0.21				68	0.40	21.8
20% Co/Al_2O_3_nf	21.8		0.33				231	0.76	13.3
30% Co/Al_2O_3_1	32.5	0.90	0.51	0.47	6.6	0.4	164	0.30	5.7
30% Co/Al_2O_3_2	33.5	0.92	0.57	0.45	6.9	0.3	149	0.31	7.9
30% Co/Al_2O_3_3	32.0		0.48				111	0.49	16.3
30% Co/Al_2O_3_4	32.4		0.63				66	0.36	21.1
30% Co/Al_2O_3_nf	32.8		0.54				202	0.59	13.0

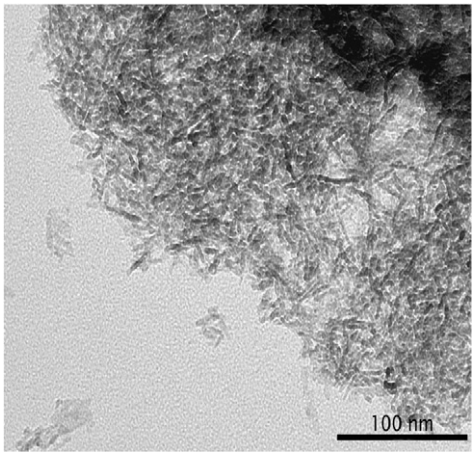

Fig. 3. Bright-field TEM image of the nanofibrous alumina at medium magnification. Individual nanofibers of ca. 2–3 × 20–50 nm are clearly observed.

of macropores detected by Hg intrusion porosimetry. Additional TEM images of the nanofibrous sample can be seen in Figs. S1e and S1f of the supporting information. No regions containing particles having distinct average dimensions nor different morphology were found within several images recorded at different positions along the TEM grid.

The texture of the surfactant-templated Al_2O_3_nf support has also been analyzed by FE-SEM. Fig. S2 of the supporting information shows a representative micrograph of the surface of the micron-sized Al_2O_3_nf particles. The existence of macropores of 80–500 nm in size is revealed in concordance with the Hg intrusion porosimetry results. This porous network appears disordered as a result of the corrugated morphology of the relatively thin macroporous walls, which are perceived in greater detail at the higher-magnification included as inset in Fig. S2. The Al_2O_3_nf support can thus be conceived as a hierarchical bimodal macro (80–500 nm)-mesoporous (16 nm) solid where the macroporous walls are constituted by randomly packed γ-Al_2O_3 nanofibers, as appraised by TEM (Fig. 3 and Figs. S1e, S1f), which are responsible for the mesoporosity detected by N_2 adsorption. This bimodal porosity is consistent with that found for similar surfactant-templated inorganic solids prepared in the presence large amounts of surfactants organized in *supermicelles* [28,38].

3.2. Characterization of RuCo/alumina catalysts

3.2.1. Elemental and chemical analyses

The nitrogen content (associated to the metal precursors) after Co and Ru impregnation and drying at 373 K as well as after the subsequent calcination at 573 K determined by elemental analysis is shown in Table 2 for samples prepared from Al_2O_3_1 and Al_2O_3_2. The amount of nitrogen in the dried solids is 5.1–5.3 wt% and 6.6–6.9 wt% for the series loaded with 20 and 30 wt% Co, respectively. After calcination the amount of nitrogen drops below 0.4 wt% in all samples, indicating a nearly complete decomposition of the metal precursors under the calcination conditions applied (573 K, 3 h).

Table 2 also collects the Co and Ru concentrations determined by ICP-OES in the calcined materials. In the case of Ru, the concentration in selected samples was also measured at different stages of catalyst preparation (dried, calcined) and after use in FTS (spent). As observed, the Co contents in the calcined solids slightly exceed the nominal values, with maximum deviations of ca. 11–12%. On the other hand, the Ru contents in the dried solids are very close to the nominal values (0.5 wt% and 1.0 wt% for 20% Co/Al_2O_3_*x* and 30% Co/Al_2O_3_*x*, respectively), but they drop by ca. 40–50% upon calcination at 573 K. A similar loss of Ru during calcination has been reported by others for Ru and bimetallic Co–Ru catalysts, and attributed to the formation of volatile suboxide species under oxygen-containing atmospheres at temperatures above 473 K [39–41]. An additional slight decrease in Ru content is noticed for the spent catalysts due to the formation of volatile ruthenium carbonyls under syngas atmosphere at the reaction conditions [42,43]. No cobalt loss was detected due to calcination or reaction, at the confidence level of the technique (±1%).

3.2.2. Nitrogen physisorption

The textural properties of the calcined catalysts as measured by N_2 physisorption are gathered in Table 2. As expected, incorporation of Co and Ru phases leads to a decrease in B.E.T. surface area and pore volume, the relative decrease being more pronounced for the series with higher metal loading (3–28% for 20 wt% Co and 6–37% for 30 wt% Co). Moreover, for each series of catalysts the relative decrease within the commercial aluminas is greater for the small pore Al_2O_3_1 and Al_2O_3_2 samples, for which a partial pore blockage by the supported metal oxide particles is more likely to occur, in agreement with previous observations [31,42]. At this point, it is worth mentioning that the relative decrease in specific surface area for the Al_2O_3_4-based catalysts is significantly lower (3–6%) than that expected from a simple dilution effect (ca. 27% and 41% decrease for catalysts with 20 wt% and 30 wt% Co, respectively) by the Co_3O_4 phase in the calcined solids if one disregards the contribution of this phase to the total specific surface area as well as the existence of any pore blockage. However, for low surface area solids such as Al_2O_3_4 (70 m^2/g), the specific external surface associated to the non-porous Co_3O_4 particles might be comparable to that of the support. For instance, spherical Co_3O_4 nanoparticles having 44 nm in diameter, which is the average Co_3O_4 particle size estimated by XRD for 20% Co/Al_2O_3_4, display a specific external surface area of 22 m^2/g which is ca. 31% of the specific surface area of the bare Al_2O_3_4 support. In this

Table 3
Cobalt dispersion and reducibility of RuCo/alumina catalysts.

Catalyst	Metal particle size				Degree of reduction[a] (%)
	XRD		H_2 chemisorption		
	$d(Co_3O_4)$ (nm)	$d(Co^0)$ (nm)	H_2 uptake (μmol/g)	$d(Co^0)$ (nm)	
20% Co/Al_2O_3_1	16.4	12.3	122	10.9	79
20% Co/Al_2O_3_2	17.3	13.0	144	11.5	92
20% Co/Al_2O_3_3	25.2	18.9	108	16.5	98
20% Co/Al_2O_3_4	44.7	33.5	70	25.2	99
20% Co/Al_2O_3_nf	14.7	11.0	164	10.2	93
30% Co/Al_2O_3_1	23.5	17.6	–	–	86
30% Co/Al_2O_3_2	26.8	20.1	–	–	95
30% Co/Al_2O_3_3	31.7	23.8	–	–	98
30% Co/Al_2O_3_4	47.9	35.9	–	–	100
30% Co/Al_2O_3_nf	16.8	12.6	–	–	95

[a] Estimated by H_2-TPR on pre-reduced (673 K, 10 h) samples (see Section 2.2.5).

case, the dilution effect becomes less relevant and the contribution of the supported Co_3O_4 phase to the total surface area of the catalyst cannot be ignored. As seen in Table 2, the catalysts based on the nanofibrous alumina do present the highest B.E.T. values within each series.

Finally, a slight decrease in the mean pore size (Table 2) and a corresponding down-shift in the pore size distribution (not shown) is observed for all the aluminas after incorporation of the metal phases without altering the order in pore sizes imposed by the corresponding pristine supports (Tables 1 and 2). Moreover, the macropore volume measured by Hg intrusion for the calcined catalysts based on the nanofibrous alumina remained almost the same than that of the bare Al_2O_3_nf support.

3.2.3. X-ray diffraction

The spinel Co_3O_4 was the only crystalline cobalt phase observed in the XRD of calcined catalysts. No diffractions corresponding to crystalline Ru phases were detected. Table 3 lists the average Co_3O_4 and Co^0 crystallite sizes obtained as explained in Section 2.2.4. As observed, the $d(Co^0)$ values estimated by XRD for catalysts based on the commercial aluminas slightly exceed the mean pore size of the corresponding supports as measured by N_2 physisorption (Table 1). This has also been previously observed by others for Co catalysts supported on SiO_2 and Al_2O_3 [32,44]. According to these studies, this observation does not exclude the location of most of the Co^0 particles inside the support pores. In fact, the formation of Co^0 particles with an elongated morphology instead of the spherical morphology assumed in the $d(Co^0)_{XRD}$ estimation has been proposed in order to explain this apparent contradiction [44]. Additionally, recent 3D-TEM studies have pointed toward an oversimplification of the pore networks in porous solids by the adsorption models applied to obtain the textural characterization data from N_2 physisorption which might also explain the dissenting values obtained by independent measurements for pore size and particle diameter [45]. Nevertheless, even if according to these recent studies it seems reasonable to assume that cobalt metal particles will be mostly located inside the support pores, the presence of a fraction of cobalt on the outer surface cannot be ruled out. It is remarkable that in the case of catalysts based on the nanofibrous alumina the average Co^0 crystallite sizes (11.0–12.6 nm) are even lower than the mean diameter of the mesopores detected by N_2 physisorption (16.1 nm). It is also evidenced in Table 3 that the average cobalt particle size increases with cobalt loading for all the aluminas used, as it has been previously observed for similar systems [36].

The unique textural properties of the nanofibrous alumina presenting simultaneously the largest specific surface area and pore size can be advantageously used to assess the real impact of both parameters on the final cobalt particle size by putting these catalysts in perspective with those based on the commercial supports for which surface area and pore size are not independent parameters. As shown in Fig. 4a, the average Co_3O_4 particle size, $d(Co_3O_4)$, for the commercial aluminas continuously increases with support pore size irrespective of metal loading, in agreement with previous studies [32,44]. This correlation, however, does not apply for catalysts based on the nanofibrous alumina as they display the lowest $d(Co_3O_4)$ at the two Co loadings despite having, in average, wider pores than the commercial samples. The lack of correlation for the nanofibrous catalysts still keeps even if only the mean pore size derived from N_2 physisorption (16.1 nm) is used to describe the porosity of the nanofibrous alumina without taking into account the contribution from macropores. By contrast, a quite satisfactory inverse relationship between $d(Co_3O_4)$ and support surface area is evidenced in Fig. 4b for all the aluminas including the nanofibrous one. Other authors have reported a direct correlation between cobalt particle size and support pore size [32,44,46,47] though in some cases [32] an obvious correlation between particle size and support surface area was not observed. In our opinion, this can be ascribed to the much more limited range of support surface areas used in those studies as compared to the present one thanks to the introduction of the original high surface area nanofibrous alumina support. The results of the present study allow us to conclude that the final cobalt dispersion is mainly determined by the specific surface area of the support rather than by its pore size.

3.2.4. Hydrogen chemisorption

Cobalt dispersion was also determined by H_2 chemisorption for the series of catalysts with 20 wt% Co loading pre-reduced at 673 K for 10 h. The results, given in Table 3, do show that the particle sizes derived from H_2 chemisorption are in reasonably harmony with those estimated by XRD. As seen in Table 3, H_2 chemisorption gives slightly lower $d(Co^0)$ values than XRD, particularly in the less dispersed 20% Co/Al_2O_3_3 and 20% Co/Al_2O_3_4 samples for which H_2 chemisorption cobalt particle sizes are about 25% lower than XRD values. Even a much better agreement between the two techniques is found in the rest of catalysts, with maximum relative differences of 12%. The good agreement between Co^0 particle sizes derived from XRD and H_2 chemisorption allow to discard any extensive cobalt sintering during the catalyst reduction treatment.

3.2.5. Transmission electron microscopy (TEM and HRTEM)

The location and size of the supported cobalt particles were examined by TEM in selected pre-reduced samples. In the case of highly dispersed catalysts, as those based on the nanofibrous alumina, slightly out-of-focus images had to be recorded to better visualize the cobalt nanoparticles due to their limited contrast against the alumina support. A representative TEM image for 20%

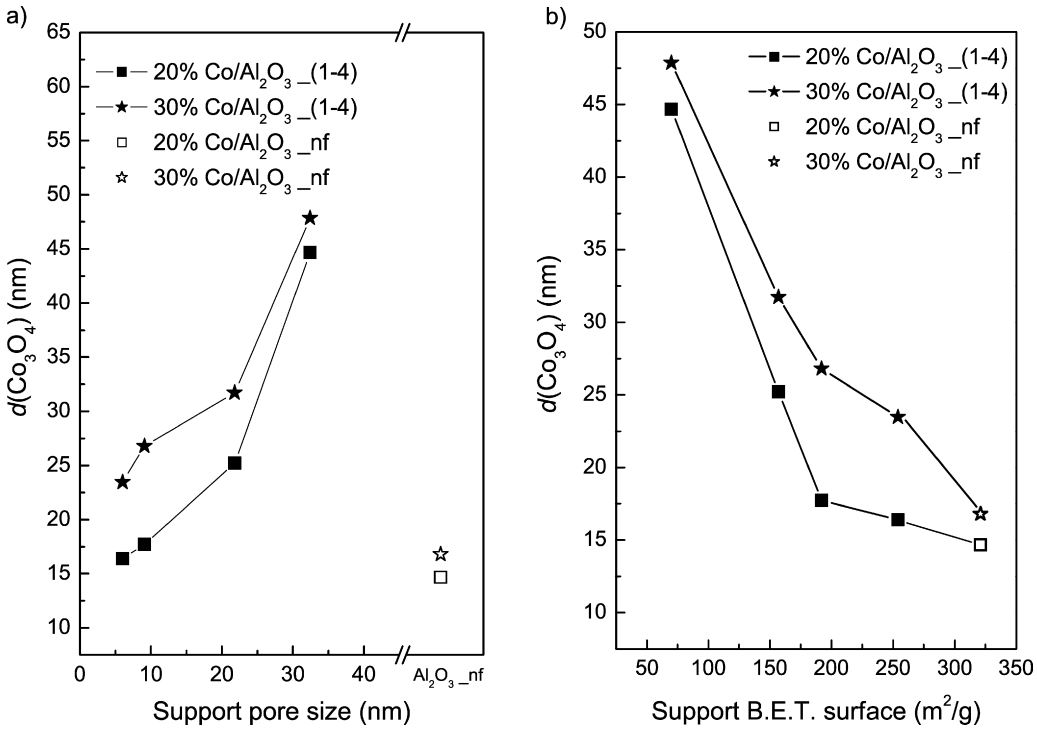

Fig. 4. Variation of cobalt oxide particle size, $d(Co_3O_4)$, with (a) pore size and (b) B.E.T. surface area of commercial (closed symbols) and nanofibrous (open symbols) alumina supports for RuCo/alumina catalysts with 20 wt% Co and 30 wt% Co loading.

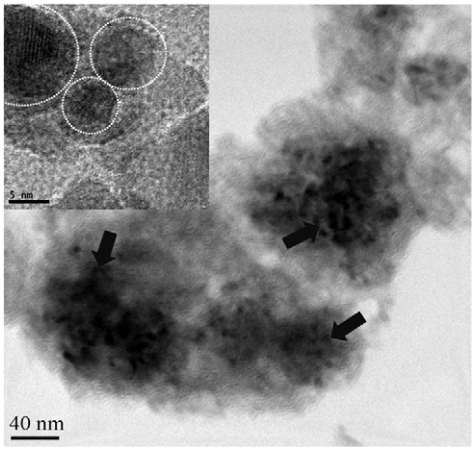

Fig. 5. Representative TEM image for 20% Co/Al_2O_3_nf catalyst. The image is recorded slightly out-of-focus for better visualizing the cobalt nanoparticles. As inset, HRTEM image evidencing the presence of very small (6–9 nm) reoxidized cobalt nanoparticles.

Co/Al_2O_3_nf sample is shown in Fig. 5. There, nearly round-shaped cobalt nanoparticles (marked with black arrows in the figure) below 8–10 nm in size coexisting with larger (10–15 nm) ones are observed, which is consistent with the mean particle size estimated by XRD and H_2 chemisorption (11.0 and 10.2 nm, respectively, Table 3). The presence of very small cobalt particles in this sample has also been evidenced by HRTEM (inset in Fig. 5), where particles sizing 6–9 nm are clearly visible, showing orientations perpendicular to the (1 1 1) crystalline plane of cubic Co^0, identified by a lattice spacing of 2.05 Å. Additionally, the characteristic lattice spacing of the (2 0 0) plane of CoO can be observed for cobalt nanoparticles below 7 nm in size, indicating that reoxidation of very small nanoparticles occurred to some extent during sample passivation, handling, and preparation prior to TEM observation. In those cases, the TEM-derived particle sizes were properly corrected to account for the size contraction related to the reduction of the CoO phase to Co^0.

3.2.6. Reducibility of catalysts

The H_2-TPR profiles for the calcined catalysts loaded with 20 wt% and 30 wt% Co are shown in Figs. 6a and 6b, respectively. For the sake of clarity, the samples in each figure have been vertically arranged according to their mean Co^0 particle size (estimated by XRD). As it is typically observed for supported Co_3O_4, all samples display two main H_2 consumption features with maxima at around 500 K ($T_{1\,max}$) and 625–670 K ($T_{2\,max}$) that correspond to the reduction of Co_3O_4 to CoO and subsequent reduction of CoO to Co^0, respectively. The H_2 consumption ratios between the second ($CoO \rightarrow Co^0$) and the first ($Co_3O_4 \rightarrow CoO$) reduction steps are systematically lower in our samples (1.7–3) than the stoichiometric ratio of 3. This is likely due to the contribution to the low temperature reduction feature of the decomposition of some residual cobalt nitrate precursor (which takes place at around 500 K on alumina [32]) remaining in the solid after calcination, as it was ascertained by elemental analysis (Table 2), and to the reduction of Ru species. The absence of reduction features above 800 K discards the formation of barely reducible cobalt aluminates in noticeable amounts, which can be attributed to the reduction promoter effect of Ru [8,48,49].

The H_2-TPR profiles shown in Figs. 6a and 6b show that, while $T_{1\,max}$ hardly varies with the Co^0 particle size within each series of catalysts prepared from the commercial aluminas, $T_{2\,max}$ shifts toward lower temperatures as the average Co^0 particle size increases. This trend concurs well with previous observations [50] and can be ascribed to a hindered reduction of smaller cobalt oxide particles displaying a stronger interaction with the surface of narrower pore aluminas. This fact also explains the lower $T_{2\,max}$ observed for the catalysts with higher Co loading having, on average, larger cobalt particle sizes (Table 3). In addition to the particle size effect (i.e. Co–support interaction), a more impeded diffusion of water molecules (formed during reduction) in narrower pores

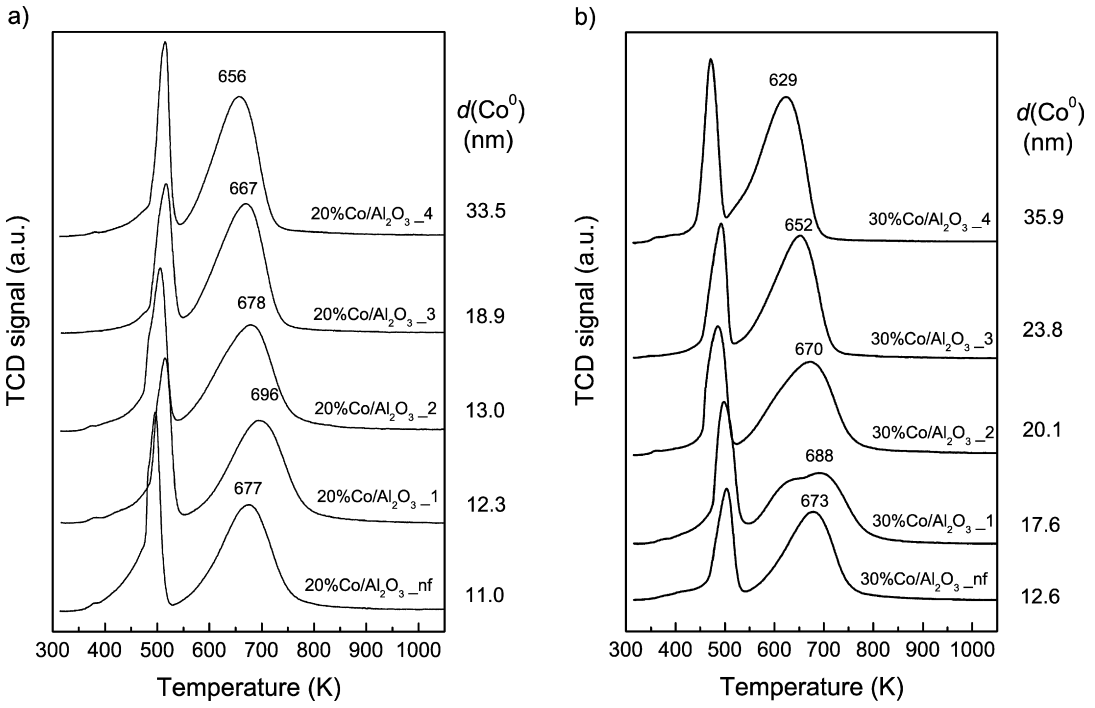

Fig. 6. H_2-TPR profiles obtained for (a) 20% Co/Al_2O_3_*x* and (b) 30% Co/Al_2O_3_*x* series of RuCo/alumina catalysts.

increasing its residence time and slowing down the reduction kinetics may also contribute to the observed reducibility trends in the commercial alumina catalysts [51,52]. Interestingly, the catalysts prepared from the nanofibrous alumina deviate from the reducibility–particle size trend observed for the commercial aluminas as the former clearly present lower $T_{2\,max}$ values (15 to 19 K depending on Co loading) than the equivalent catalysts based on the smallest pore size Al_2O_3_1 alumina while having lower cobalt particle sizes. This anomalous behavior can be explained by the original hierarchical bimodal porosity of the Al_2O_3_nf support having a significant contribution of large macropores that facilitate the removal of water from the catalyst pores during the reduction process. Therefore, the reduction kinetics and, consequently, the overall extent of reduction in supported Co catalysts is determined by a combined effect of cobalt particle size (cobalt–support interaction strength) and support porosity (water diffusion effect). This conclusion has been made possible thanks to the use of the original catalysts based on the nanofibrous alumina as they display opposite extreme values in pore size and cobalt particle size within the series of catalysts studied.

The degrees of cobalt reduction after the reduction treatment at 673 K for 10 h in pure H_2 (see experimental conditions in Section 3.2.6) are collected in Table 3. As seen there, degrees of reduction of 80–100% are observed for all samples, and thus only a small amount of non-reduced cobalt phases is expected to exist in the reduced catalysts. A clear parallelism between the degrees of reduction at 673 K given in Table 3 and the $T_{2\,max}$ values in the respective H_2-TPR profiles corresponding to the second cobalt reduction step ($CoO \rightarrow Co^0$) (Figs. 6a and 6b) is observed, that is, lower $T_{2\,max}$ values do correspond with higher extents of reduction. Thus, samples based on Al_2O_3_1 are those displaying the lowest degrees of reduction (79–86%) and the highest $T_{2\,max}$ values (696–688 K) while the opposite holds for the catalysts based on the wider pore Al_2O_3_4 alumina (99–100% degrees of reduction and $T_{2\,max} = 656$–629 K).

The characterization results discussed above have shown that the original morphology of the nanofibrous alumina leads to catalysts presenting both the highest porosity and the highest cobalt dispersion. This particular property is expected to shed light on the relative impact of diffusion and dispersion effects on FTS catalyst performance when these catalysts are put in perspective with those obtained from the commercial aluminas. These aspects will be discussed in detail in the following sections.

3.3. Fischer–Tropsch synthesis

3.3.1. Transitory behavior

All the RuCo/alumina catalysts studied experienced changes in activity and selectivity during the initial stages of the FTS (transitory state) until a *pseudo*-steady state behavior is attained at time-on-stream (TOS) above 7–8 h. As will be shown here, the behavior of the catalysts during both the transitory and *pseudo*-steady states is strongly dependent on the textural properties of the alumina supports.

Fig. 7 shows the evolution of the cobalt-time-yield and the olefin-to-paraffin (O/P) weight ratio for hydrocarbons in the C_5–C_7 range with TOS for 20% Co/Al_2O_3_1, 20% Co/Al_2O_3_4, and 20% Co/Al_2O_3_nf catalysts. A larger initial decrease in cobalt-time-yield is observed for 20% Co/Al_2O_3_1 prepared from the smaller pore commercial alumina (Fig. 7a) as compared to the wider pore 20% Co/Al_2O_3_4 catalyst (Fig. 7b). Interestingly, the change of the O/P ratio with TOS in these two catalysts parallels that of the cobalt-time-yield. Intermediate behaviors were observed for the commercial samples with intermediate pore sizes (not shown). The augment of the relative change in activity and O/P ratio during the transitory period from 20% Co/Al_2O_3_1 to 20% Co/Al_2O_3_4 reflects the increasing resistance to the diffusion of CO and α-olefins through the waxy liquid phase filling the catalyst pores (which develops during the first stages of the reaction) with decreasing the mean pore size of the alumina support [13,14,53]. On the other hand, the catalyst based on the nanofibrous alumina displays a low relative decrease in the cobalt-time-yield during the initial stages (Fig. 7c) and in this respect it behaves like the wider pore 20% Co/Al_2O_3_4 catalyst. Conversely, the O/P ratio in 20% Co/Al_2O_3_nf sharply declines during the transitory stage, resembling the behavior of the small pore 20% Co/Al_2O_3_1 sample. This fact may

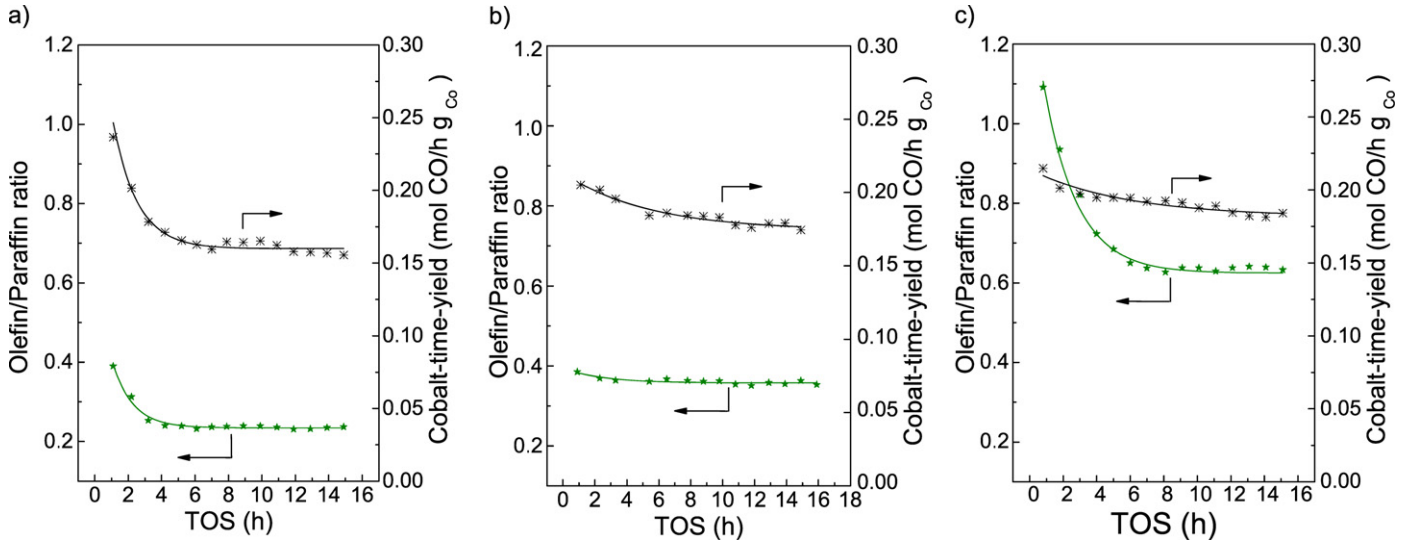

Fig. 7. Change of the cobalt-time-yield and paraffin-to-olefin weight ratio for hydrocarbons in the C_5–C_7 range for selected catalysts: (a) 20% Co/Al_2O_3_1, (b) 20% Co/Al_2O_3_4, and (c) 20% Co/Al_2O_3_nf (nanofibrous).

be explained by taking into account the bimodal porosity of the nanofibrous alumina containing both mesopores of ca. 16 nm in diameter and large macropores, as previously discussed. Thus, the sharp initial decrease in the O/P ratio observed for this sample is likely due to the enhanced restriction for the diffusion of α-olefins in the mesopores of Al_2O_3_nf. However, it is worth to mention here that the absolute value for the O/P ratio attained after the transitory state is significantly higher for the nanofibrous catalyst (O/P $\sim$ 0.6) as compared to the wider pore commercial alumina (O/P $\sim$ 0.4), which clearly indicates a lower barrier for the diffusion of α-olefins in the former, due to its macroporous network. These results unambiguously show that the diffusion of both CO and α-olefins through the liquid hydrocarbon layer surrounding the Co^0 particles is significantly enhanced in the macro-mesoporosity of the nanofibrous alumina support as compared to the commercial aluminas.

3.3.2. Pseudo-stationary state

A catalyst will work under the so-called *pseudo*-stationary state during most of its lifetime and, thus, it is of prime importance to determine the implications of support texture and cobalt dispersion on the specific catalyst activity and product distribution in this stage. As it was mentioned above, the absolute values of the O/P ratio in the *pseudo*-stationary state are directly related to the restriction for the diffusion of α-olefins through the pores of a working catalyst and thus to the textural characteristics of the alumina support. This is clearly seen in Fig. 8, where the O/P weight ratio in the *pseudo*-stationary state for individual C_5, C_7, and C_9 hydrocarbons has been plotted against the support pore size for the series loaded with 20 wt% Co. For all catalysts the O/P ratio decreases with increasing the hydrocarbon chain length from C_5 to C_9 due to the increase in the residence time of the longer α-olefins in the pores and thus of the probability for their re-adsorption, incorporation into growing chains, and subsequent desorption through hydrogenation as paraffins [13]. Moreover, for a given hydrocarbon chain length the O/P ratio is seen to increase with the support pore size evidencing a higher transport rate of the α-olefins in larger pores. For the commercial aluminas this effect is more noticeable in the range of pore sizes from 6.0 to 9.1 nm and becomes smoother for larger pore sizes. On the other hand, the catalyst prepared from the macro-mesoporous nanofibrous alumina displays, by far, the highest O/P ratios irrespective of the hydrocarbon chain length, clearly manifesting the important contribution of the macropores present in this support for rapidly evacuating the α-olefins and inhibiting their re-adsorption and hydrogenation on the active sites. These results substantiate the consideration of the nanofibrous alumina as that displaying the largest pore size (see Section 3.1.2).

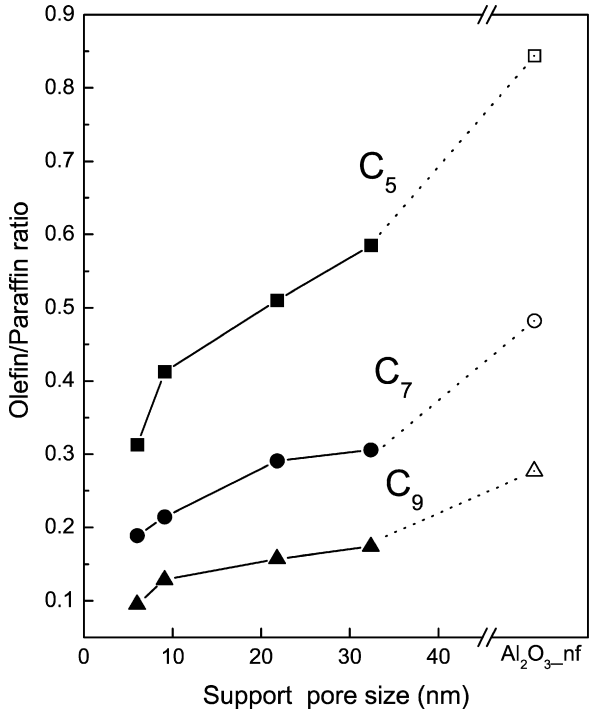

Fig. 8. *Pseudo*-steady state olefin-to-paraffin (O/P) weight ratios for individual C_5, C_7, and C_9 hydrocarbons as a function of support pore size for the 20% Co/Al_2O_3_x catalyst series.

Besides pore size-related intrapellet diffusional issues, the possible affect of cobalt dispersion (i.e. particle size) on product selectivity has been a matter of interest and discussion during the last decades [16–18,54,55]. For instance, an increased selectivity lo light hydrocarbons, particularly to CH_4, has been reported for highly dispersed catalysts containing very small cobalt particles [17,18]. However, extracting definitive conclusions regarding the real impact of dispersion on the selectivity of a working catalyst from

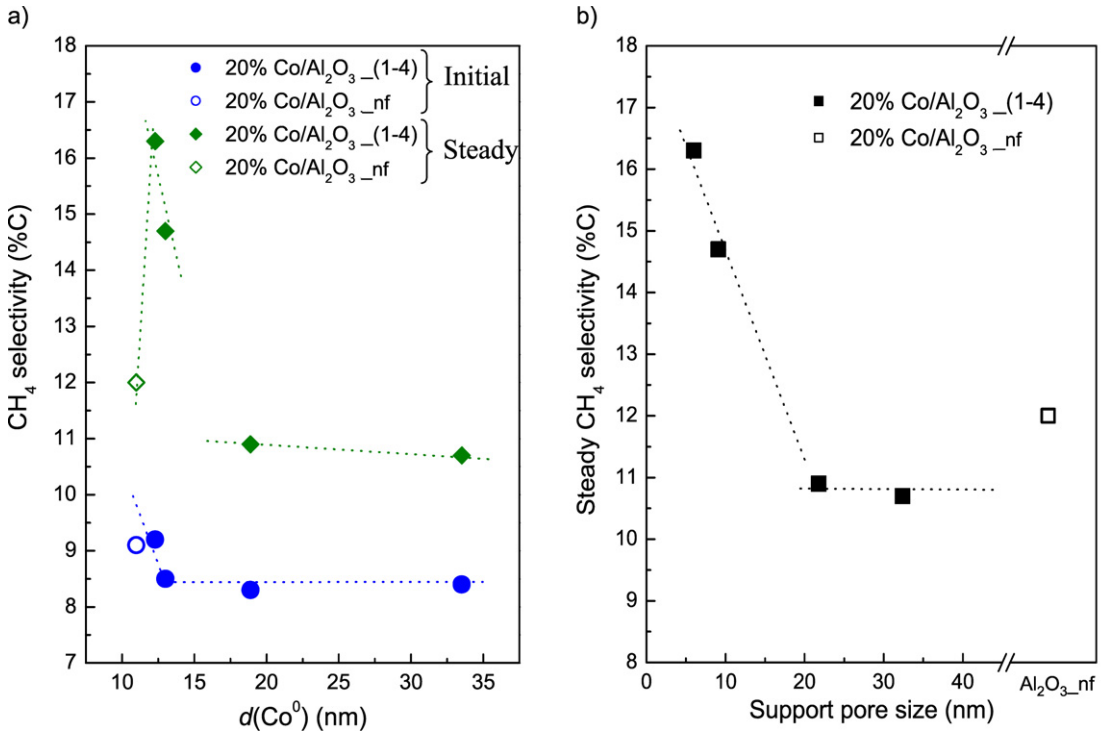

Fig. 9. (a) Initial and *pseudo*-steady methane selectivities as a function of Co^0 particle size, and (b) *pseudo*-steady methane selectivities against support pore size, for 20% Co/Al_2O_3_*x* series of catalysts. Open symbols correspond to the nanofibrous alumina catalysts.

previous works is intricate owing to the difficulty in splitting dispersion and pore size (i.e. diffusion) effects, as both parameters are closely interrelated in supports with conventional morphology. This is particularly so for large catalyst pellets (>0.1 mm) applied in fixed bed reactors since, as discussed earlier, the product transport rate through the catalyst pores has a non-negligible contribution to product selectivity. In the present study, the singular morphology of the nanofibrous alumina support leading to catalysts displaying both the highest cobalt dispersion (Table 3) and the lowest diffusional restrictions (Fig. 8) within the series of catalysts studied, together with a very high cobalt reducibility, may help in elucidating the relative impact of these two parameters on selectivity. In the following discussions, XRD-derived Co^0 particles sizes will be used for convenience as no particle sizes obtained by H_2 chemisorption are available for the series of catalysts loaded with 30 wt% Co, although identical conclusions would emerge by using H_2-chemisorption particle sizes due to the already mentioned good correspondence between both characterizations.

The initial (extrapolated at zero TOS) and *pseudo*-steady state methane selectivities are plotted in Fig. 9a as a function of cobalt particle size for the 20% Co/Al_2O_3_*x* series of catalysts. The initial (thus in the absence of diffusional issues) CH_4 selectivity is seen to remain almost invariable at around 8.3–8.5% C for $d(Co^0)$ in the range of 13.0–33.5 nm, while slightly higher values (9.1–9.2% C) are observed for the more dispersed catalysts derived from the smaller pore commercial (Al_2O_3_1) and the nanofibrous (Al_2O_3_nf) aluminas. This result is explained by the intrinsically higher methane selectivity of Co^0 nanoparticles below ca. 10 nm in size [18] which should be present in a non-negligible amount in these two catalysts (as confirmed by TEM-HRTEM in the nanofibrous one, Fig. 5) displaying the highest metal dispersions with mean Co^0 particle sizes of 10–12 nm according to both XRD and H_2 chemisorption measurements (Table 3).

As seen in Fig. 9a, methane selectivities in the *pseudo*-steady state are systematically higher and experience more drastic changes with particle size (in the range below ca. 20 nm) than the initial ones. Moreover, no apparent correlation between *pseudo*-steady CH_4 selectivity and $d(Co^0)$ is found when the nanofibrous catalyst is included in the comparison, as shown by the dashed guide lines in Fig. 9a. By contrast, a more clear correlation comes out when the *pseudo*-steady CH_4 selectivity is plotted as a function of support pore size (Fig. 9b). For the commercial alumina catalysts, the methane selectivity sharply declines from 16.3 to 10.9% C when increasing the mean pore size from 6.0 to 21.8 nm and then remains almost invariant for larger pore sizes. The nanofibrous alumina roughly follows the selectivity–pore size correlation, though it displays a slightly higher methane selectivity than the wider pore commercial aluminas, despite the former provides the easiest intrapellet diffusion, as already discussed. This fact might be ascribed to the intrinsic higher methane selectivity of the very small (<10 nm) cobalt nanoparticles, also perceived in the absence of diffusional issues, at zero TOS (Fig. 9a). These results, together with the fact that methane selectivity was reported to remain invariable with TOS under conditions where no reactant diffusion limitations exist [14], strongly point toward the predominant role of diffusional issues in determining product selectivity in a working catalyst. Thus, the selectivity trend shown in Fig. 9b can be accounted for by considering the increase in the CO-diffusion limitation and consequently in the local H_2/CO ratio near the Co^0 active sites when decreasing the support pore size.

The initial and steady cobalt-time-yields and the initial turnover frequencies (TOF) obtained for the two series of $RuCo/Al_2O_3$ catalysts are gathered in Table 4. The initial (in the absence of diffusional restrictions) cobalt-time-yield for the catalysts prepared from the commercial aluminas generally decreases with increasing the support pore size and cobalt loading due to the decrease in cobalt dispersion. Sample 20% Co/Al_2O_3_1, however, displays a slightly lower cobalt-time-yield than 20% Co/Al_2O_3_2 despite its higher dispersion (Table 3), which may be attributed to the lower cobalt reducibility (79% against 92%, see Table 3) and to a higher relative population of very small Co^0 nanoparticles (displaying lower TOFs than larger ones [18,56]) in the former. The size-

Table 4
Initial and *pseudo*-steady FTS activity of RuCo/alumina catalysts.

Catalyst	Cobalt-time-yield[a] (mol CO/g_{Co} h)			Initial TOF[c] (10^{-2} s^{-1})
	Initial	Steady	Yield loss[b] (%)	
20% Co/Al_2O_3_1	0.271	0.153	43.5	6.2 (6.2)
20% Co/Al_2O_3_2	0.285	0.202	30.0	6.6 (5.9)
20% Co/Al_2O_3_3	0.260	0.205	21.2	8.2 (7.2)
20% Co/Al_2O_3_4	0.223	0.185	17.0	11.8 (9.3)
20% Co/Al_2O_3_nf	0.225	0.183	18.7	4.2 (4.5)
30% Co/Al_2O_3_1	0.215	0.128	40.5	7.1
30% Co/Al_2O_3_2	0.204	0.132	35.3	7.2
30% Co/Al_2O_3_3	0.202	0.150	25.7	8.1
30% Co/Al_2O_3_4	0.151	0.125	17.2	8.9
30% Co/Al_2O_3_nf	0.224	0.177	21.0	5.0

[a] Fischer–Tropsch reaction conditions: $T = 493$ K, $P = 2.0$ MPa, $H_2/CO = 2$.
[b] Relative loss of cobalt-time-yield from the initial (TOS → 0) to the *pseudo*-stationary state (TOS > 8 h).
[c] Calculated from XRD Co^0 particle sizes, cobalt content, and degrees of reduction (Table 3). Data in parenthesis correspond to TOFs based on H_2 chemisorption.

dependent activity of Co^0 particles also accounts for the relatively low initial cobalt-time-yield displayed by the highly reducible nanofibrous 20% Co/Al_2O_3_nf catalyst having a slightly lower mean Co^0 particle size than 20% Co/Al_2O_3_1. However, the nanofibrous 30% Co/Al_2O_3_nf catalyst turns out to be, initially, the most active one among the catalysts with 30 wt% Co loading, thanks to its highest dispersion and to the shift toward higher particle sizes (lowering the population of less active very small nanoparticles) with increasing cobalt loading (Table 3). The effect of the particle size-dependent FTS activity is clearly reflected in the initial TOF values given in the last column of Table 4 and their change with Co^0 particle size (Fig. 10). As seen there, the initial TOF for all catalysts in the two series noticeably increases with the mean Co^0 particle size in the low particle size range (<15 nm) where the population of less active small nanoparticles in the catalysts, especially in those prepared from the nanofibrous alumina, should be higher. Changes in TOF are much less pronounced for larger metal particles, approaching a plateau for sizes above 20 nm, in good agreement with the TOF–particle size dependence for very small (<10 nm) nanoparticles as recently reported by Bezemer et al. [18] and the invariant TOF found by Iglesia et al. [15] for $d(Co^0) > 10$–12 nm. It is worth to mention that the same trend is observed when TOFs are calculated from H_2 chemisorption data (as seen in Table 4 for 20% Co/Al_2O_3_x samples).

As shown in Table 4, the relative loss of cobalt-time-yield from the initial reaction stage (TOS → 0) to the *pseudo*-steady state continuously increases from ca. 17 to 43% with decreasing the support pore size in the commercial alumina catalysts. The catalysts prepared from the nanofibrous alumina behave, as expected from their textural characteristics, as a wide pore support with relative decreases in activity of ca. 19% and 21% at 20 wt% and 30 wt% Co loading, respectively. These trends can be related to the increase in the CO transport rate from the gas phase to the active sites through the liquid hydrocarbon phase filling the catalyst pores with increasing the support pore size, as discussed earlier. Thanks to its high initial cobalt-time-yield and low relative loss of activity during the transitory stage, the nanofibrous 30% Co/Al_2O_3_nf catalyst displays the highest steady activity within the 30% Co/Al_2O_3_x series, with a time-yield of 0.177 $mol_{CO}/(g_{Co}\,h)$ about 20% higher than that of the most active 30% Co/Al_2O_3_3 sample (time-yield of 0.150 $mol_{CO}/(g_{Co}\,h)$) within the commercial aluminas.

The *pseudo*-steady selectivities to the different hydrocarbon fractions at 40% CO conversion are given in Table 5. As observed, the steady selectivity to long-chain C_{13+} hydrocarbons (including the most interesting diesel, C_{13}–C_{22}, and C_{23+} waxes) for the commercial alumina catalysts increases with the mean support pore size irrespective of cobalt loading. For these catalysts the structural parameter χ, as defined by Iglesia et al. [13], is in the range

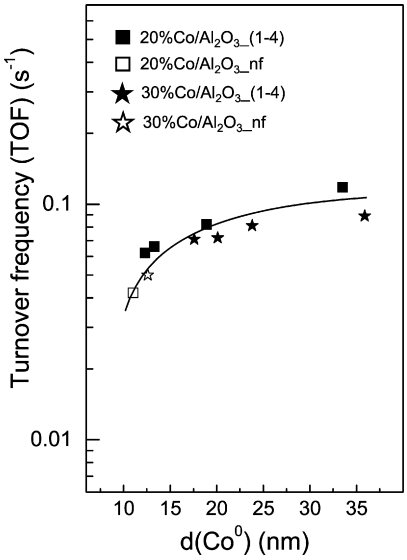

Fig. 10. Change of the initial *turnover frequency* (TOF) with Co^0 particle size for 20% Co/Al_2O_3_x and 30% Co/Al_2O_3_x series of catalysts. Open symbols correspond to the nanofibrous alumina catalysts.

113×10^{16}–1350×10^{16} m^{-1} where product selectivity is controlled by the intrapellet CO diffusion to the active sites [13]. Thus, the increase in C_{13+} selectivity with the pore size of commercial alumina supports is a consequence of the more favorable H_2/CO ratio near the active sites produced by the enhanced CO transport rate in larger pores and its impact on the chain growth kinetics displaying a positive order with respect to CO fugacity [53]. On the other hand, the nanofibrous alumina catalysts display a C_{13+} selectivity lower than that of the large pore Al_2O_3_3 and Al_2O_3_4 commercial aluminas, despite the former should also provide an easy access of CO to the active sites according to their low relative loss of activity during the initial reaction stages (Fig. 7c, Table 4). This evidences that other factors besides diffusion-related phenomena have an affect on the steady FTS selectivity. In this respect, an enhanced selectivity to heavy hydrocarbons has been reported for Co catalysts in the absence of diffusional restrictions with increasing cobalt particle size [18,32]. Similarly, a very high selectivity to long-chain hydrocarbons is claimed in a recent patent for cobalt supported on a partially or totally crystallized α-Al_2O_3 having very low surface area (15–70 m^2/g) and thus poor cobalt dispersion [57]. Accordingly, the higher C_{13+} selectivity displayed by the catalysts based on the large pore (low surface area) commercial aluminas can be ascribed to the contribution of the large cobalt particles prevailing in these less dispersed catalysts. Then, it

Table 5
Hydrocarbon product distribution for RuCo/alumina catalysts at 40% CO conversion.

Catalyst	Hydrocarbon distribution (% C)					Productivity to diesel (10^{-4} mol C/g_{cat} h)
	C_1	C_2–C_4	C_5–C_{12}	C_{13+}	C_{23+}/C_{13+} ratio	
20% Co/Al_2O_3_1	16.3	12.1	40.8	30.8	0.22	76
20% Co/Al_2O_3_2	14.7	12.8	40.9	31.5	0.28	101
20% Co/Al_2O_3_3	10.9	9.9	39.0	40.2	0.34	121
20% Co/Al_2O_3_4	10.7	8.7	33.3	47.3	0.38	118
20% Co/Al_2O_3_nf	12.0	12.5	40.0	35.5	0.29	101
30% Co/Al_2O_3_1	15.6	15.3	50.8	18.3	0.15	65
30% Co/Al_2O_3_2	14.7	16.2	43.7	25.4	0.16	94
30% Co/Al_2O_3_3	12.8	10.6	38.9	37.7	0.32	123
30% Co/Al_2O_3_4	11.1	9.0	34.3	45.6	0.37	116
30% Co/Al_2O_3_nf	13.8	13.2	38.8	34.2	0.29	141

can be concluded from the above results that two factors directly influence the steady state selectivity to the desired long-chain hydrocarbons: the actual H_2/CO ratio at the active sites controlled by the CO intrapellet diffusion, and the cobalt particle size (i.e. dispersion) mainly governed by the surface area of the alumina support (Fig. 4b). At this point it should be mentioned that the slightly lower C_{13+} selectivities systematically observed for the 30 wt% Co catalysts as compared to the 20 wt% counterparts (Table 5) are likely related to the higher (around 30%) space velocity required for the former samples to attain the target 40% CO conversion which, in turn, causes a decrease in the average bed residence time for α-olefins and forces to analyze separately the two series of catalysts. Much smaller variations in GHSV (in the range of 3.5–6%) were required to attain the 40% conversion level within the 20 and 30 wt% Co series as the differences in activity for catalysts within each series are diminished after the transitory stage, thus discarding any remarkable affect of this parameter on product selectivity.

Finally, the C_{23+}/C_{13+} ratios shown in Table 5 indicate that the very large cobalt particles prevailing in the large pore Al_2O_3_3 and Al_2O_3_4 based catalysts do promote the formation of waxes (C_{23+}) with respect to catalysts based on the small pore commercial aluminas and the nanofibrous one. By contrast, the latter are more selective toward the desired diesel-range (C_{13}–C_{22}) products within the C_{13+} fraction, revealing that formation of diesel products becomes favored when the chain-growth processes are promoted only by the absence of a H_2-enrichment at the active sites (large porosity and high dispersion, as in the nanofibrous catalysts) than when this effect is accompanied by the presence of very large cobalt particles (large porosity and poor dispersion, as in Al_2O_3_3 and Al_2O_3_4 based catalysts). As a result of its high cobalt-time-yield, high stability with TOS, and good diesel selectivity, the nanofibrous catalyst with 30 wt% Co loading is that giving the highest productivity to diesel (141 mol/(g_{cat} h)) among all catalysts studied (Table 5).

4. Conclusions

By taking advantage of the unique textural properties of γ-Al_2O_3 nanofibers presenting simultaneously very high surface area (321 m^2/g) and a hierarchical macro-mesoporous structure, supported CoRu catalysts have been prepared at two loading levels (20 wt% Co–0.5 wt% Ru and 30 wt% Co–1.0 wt% Ru) and used to elucidate the relative significance of diffusional and dispersion effects during FTS by putting them in perspective with equivalent catalysts prepared from commercial aluminas (Sasol) with different pore sizes (6–32 nm). The introduction of the original nanofibrous catalysts allowed to conclude that the final cobalt dispersion in RuCo/γ-Al_2O_3 catalysts is mainly controlled by support surface area rather than by pore size. It has been shown that the initial (thus in the absence of diffusional issues) FTS activity and selectivity is mostly determined by Co^0 dispersion and the related non-classical particle size effects (lower TOF and higher CH_4 selectivity for Co^0 nanoparticles below 8–10 nm in size) previously reported [18]. By contrast, catalyst porosity becomes the most relevant parameter determining the catalyst performance in the *pseudo*-steady state (TOS > 7–8 h) reflecting the kinetic relevance of reactants (CO) and products (α-olefins) diffusional steps. Thus, the very open porous structure of the nanofibrous alumina provides an enhanced CO intrapellet diffusion to the active sites resulting in a relatively low activity loss during the transitory period (TOS < 7–8 h). The benefits of using the macro-mesoporous nanofibrous support (high Co^0 dispersion and fast CO transport rate through the liquid phase filling the pores) are manifested at high metal loadings (30 wt% Co) where the nanofibrous catalyst displays the highest specific activity and productivity to diesel products. In contrast, waxy hydrocarbons (C_{23+}) are favored in catalysts prepared from wide pore commercial aluminas due to the intrinsically high wax selectivity of very large Co^0 nanoparticles prevailing in these less dispersed materials.

Acknowledgments

Financial support by the Comisión Interministerial de Ciencia y Tecnología of Spain (project CTQ2007-66614/PPQ) is gratefully acknowledged. We also thank Sasol for kindly supplying the commercial aluminas, Dr. S. Agouram and P. Gómez (UV) for their assistance with TEM and SEM characterizations, Dr. M. Faraldos (ICP-CSIC) for Hg intrusion porosimetry experiments, and Dr. M.A. Arribas (ITQ) for performing H_2 chemisorption measurements. G. Prieto thanks the Ministerio de Educación y Ciencia of Spain for a Ph.D. scholarship.

Supporting information

The online version of this article contains additional supporting information.

Please visit DOI: 10.1016/j.jcat.2009.02.021.

References

[1] I. Wender, Fuel Process. Technol. 48 (1996) 189.
[2] J.H. Gregor, Catal. Lett. 7 (1990) 317.
[3] E. Iglesia, Appl. Catal. A 161 (1997) 59.
[4] M.E. Dry, Catal. Today 6 (1990) 183.
[5] H.M.H. van Wechem, M.M.G. Senden, Stud. Surf. Sci. Catal. 81 (1994) 43.
[6] E. Iglesia, Stud. Surf. Sci. Catal. 107 (1997) 153.
[7] S. Strorsæter, B. Tøtdal, J.C. Walmsley, B.S. Tanem, A. Holmen, J. Catal. 236 (2005) 139.
[8] E. Iglesia, S.L. Soled, R.A. Fiato, G.H. Via, J. Catal. 143 (1993) 345.
[9] D. Wei, J.G. Goodwin, R. Oukaci, A.H. Singleton, Appl. Catal. A 210 (2001) 137.
[10] A.A. Adesina, Appl. Catal. A 138 (1996) 345.
[11] J.F. Shultz, M. Abelson, K.C. Stein, R.B. Anderson, J. Phys. Chem. 63 (1959) 496.
[12] R.B. Anderson, L.J.E. Hofer, J. Chem. Eng. Data 5 (1960) 511.
[13] E. Iglesia, S.C. Reyes, R.J. Madon, J. Catal. 129 (1991) 238.
[14] R.J. Madon, E. Iglesia, J. Catal. 149 (1994) 428.

[15] E. Iglesia, S.L. Soled, R.A. Fiato, J. Catal. 137 (1992) 212.
[16] S.W. Ho, M. Houlalla, D.M. Hercules, J. Phys. Chem. 94 (1990) 6396.
[17] A. Barbier, A. Tuel, I. Arcon, A. Kodre, G.A. Martin, J. Catal. 200 (2001) 106.
[18] G.L. Bezemer, J.H. Bitter, H.P.C.E. Kuipers, H. Oosterbeek, J.E. Holewijn, X. Xu, F. Kapteijn, A.J. van Dillen, K.P. de Jong, J. Am. Chem. Soc. 128 (2006) 3956.
[19] J.-S. Girardon, E. Quinet, A. Griboval-Constant, P.A. Chernavskii, L. Gengembre, A.Y. Khodakov, J. Catal. 248 (2007) 143.
[20] Y. Wu, G. Cheng, K. Katsov, S.W. Sides, J. Wang, J. Tang, G.H. Fredrickson, M. Moscovits, G.D. Stucky, Nat. Mater. 3 (2004) 816.
[21] X. Chen, M. Knez, A. Berger, K. Nielsch, U. Gösele, M. Steinhart, Angew. Chem. Int. Ed. 46 (2007) 6829.
[22] H.C. Lee, H.J. Kim, S.H. Chung, K.H. Lee, H.C. Lee, J.S. Lee, J. Am. Chem. Soc. 125 (2003) 2882.
[23] H.C. Lee, H.J. Kim, C.H. Rhee, K.H. Lee, J.S. Lee, S.H. Chung, Micropor. Mesopor. Mater. 79 (2005) 61.
[24] H.Y. Zhu, J.D. Riches, J.C. Barry, Chem. Mater. 14 (2002) 2086.
[25] Y. Lan, X. Gao, H. Zhu, Z. Zheng, T. Yan, F. Wu, S.P. Ringer, D. Song, Adv. Funct. Mater. 15 (2005) 1310.
[26] K. Zhou, X. Wang, X. Sun, Q. Peng, Y. Li, J. Catal. 229 (2005) 206.
[27] G. Glaspell, H.M.A. Hassan, A. Elzatahry, L. Fuoco, N.R.E. Radwan, M.S. El-Shall, J. Phys. Chem. B 43 (2006) 21387.
[28] T.-Z. Ren, Z.-Y. Yuan, B.-L. Su, Langmuir 20 (2004) 1531.
[29] B. Tang, J. Ge, L. Zhuo, G. Wang, J. Niu, Z. Shi, Y. Dong, Eur. J. Inorg. Chem. (2005) 4366.
[30] F. Vaudry, S. Khodabandeh, M.E. Davis, Chem. Mater. 8 (1996) 1451.
[31] H.Y. Zhu, X.P. Gao, D.Y. Song, Y.Q. Bai, S.P. Ringer, Z. Gao, Y.X. Xi, W. Martens, J.D. Riches, R.L. Frost, J. Phys. Chem. B 108 (2004) 4245.
[32] Ø. Borg, S. Eri, E.A. Blekkan, S. Storsæter, H. Wigum, E. Rytter, A. Holmen, J. Catal. 248 (2007) 89.
[33] K.S.W. Sing, D.H. Everett, R.A.W. Haul, L. Moscou, R.A. Pierotti, J. Rouquérol, T. Siemieniewska, Pure Appl. Chem. 57 (4) (1985) 603.
[34] D. Schanke, S. Vada, E.A. Blekkan, A.M. Hilmen, A. Hoff, A. Holmen, J. Catal. 156 (1995) 85.
[35] R.C. Reuel, C.H. Bartholomew, J. Catal. 85 (1984) 63.
[36] A. Martínez, C. López, F. Márquez, I. Díaz, J. Catal. 220 (2003) 486.
[37] A. Martínez, J. Rollán, M.A. Arribas, H.S. Cerqueira, A.F. Costa, E.F.S. Aguiar, J. Catal. 249 (2007) 160.
[38] J.-L. Blin, A. Léonard, Z.-Y. Yuan, L. Gigot, A. Vantomme, A.K. Cheetham, B.-L. Su, Angew. Chem. Int. Ed. 42 (2003) 2872.
[39] W. Zou, R.D. González, Catal. Today 15 (1992) 443.
[40] T. López, L. Herrera, R. Gómez, W. Zou, K. Robinson, R.D. González, J. Catal. 136 (1992) 621.
[41] J.-S. Girardon, E. Quinet, A. Griboval-Constant, P.A. Chernavskii, L. Gengembre, A.Y. Khodakov, J. Catal. 248 (2007) 143.
[42] J.G. Goodwin, D.O. Goa, S. Erdal, F.H. Rogan, Appl. Catal. 24 (1986) 199.
[43] S. Uchiyama, B.C. Gates, J. Catal. 110 (1988) 388.
[44] A.Y. Khodakov, A. Griboval-Constant, R. Bechara, V.L. Zholobenko, J. Catal. 206 (2002) 230.
[45] S. Storsæter, Ø. Borg, E.A. Blekkan, A. Holmen, J. Catal. 231 (2005) 405.
[46] H. Xiong, Y. Zhang, S. Wang, J. Li, Catal. Commun. 6 (2005) 512.
[47] A.M. Saib, M. Caeys, E. van Steen, Catal. Today 71 (2002) 395.
[48] A. Kogelbauer, J.G. Goodwin Jr., R. Oukaci, J. Catal. 160 (1996) 125.
[49] N. Tsubaki, S. Sun, K. Fujimoto, J. Catal. 199 (2001) 236.
[50] A.Y. Khodakov, A. Griboval, R. Bechara, F. Villain, J. Phys. Chem. B 105 (2001) 9805.
[51] J. Panpranot, J.G. Goodwin Jr., A. Sayari, Catal. Today 77 (2002) 269.
[52] P. Concepción, C. López, A. Martínez, V.F. Puntes, J. Catal. 228 (2004) 321.
[53] C.S. Kellner, A.T. Bell, J. Catal. 70 (1981) 418.
[54] A.S. Lisitsyn, A.V. Golovin, V.L. Kutnetsov, Y.I. Yermanov, J. Catal. 95 (1985) 433.
[55] B.G. Johnson, C.H. Bartholomew, D.W. Goodman, J. Catal. 128 (1991) 231.
[56] A. Martínez, G. Prieto, J. Catal. 245 (2007) 470.
[57] S. Eri, J. Kinnari, D. Schanke, A.-M. Hilmen, US Patent 0077737 (2004).